

Pressure-induced structural modulations in coesite

Ye Wu,^{1,*} Hanyu Liu,^{2,3,4,†} Haijun Huang,¹ Yingwei Fei,⁴ Xiaolei Feng,^{5,6} and Simon A. T. Redfern^{5,6,‡}

¹*School of Science, Wuhan University of Technology, Wuhan, Hubei 430070, China*

²*Innovation Center for Computational Physics Method and Software, College of Physics, Jilin University, Changchun 130012, China*

³*State Key Laboratory of Superhard Materials, College of Physics, Jilin University, Changchun 130012, China*

⁴*Geophysical Laboratory, Carnegie Institution for Science, Washington, DC 20015, USA*

⁵*Center for High Pressure Science and Technology Advanced Research (HPSTAR), Shanghai 201203, China*

⁶*Department of Earth Sciences, University of Cambridge, Downing Street, Cambridge CB2 3EQ, United Kingdom*

HPSTAR
635-2018

 (Received 26 January 2018; revised manuscript received 16 August 2018; published 20 September 2018)

Silica phases, SiO₂, have attracted significant attention as important phases in the fields of condensed-matter physics, materials science, and (in view of their abundance in the Earth's crust) geoscience. Here, we experimentally and theoretically demonstrate that coesite undergoes structural modulations under high pressure. Coesite transforms to a distorted modulated structure, coesite-II, at 22–25 GPa with modulation wave vector $q = 0.5b^*$. Coesite-II displays further commensurate modulation along the y axis at 36–40 GPa and the long-range ordered crystalline structure collapses beyond ~ 40 GPa and starts amorphizing. First-principles calculations illuminate the nature of the modulated phase transitions of coesite and elucidate the modulated structures of coesite caused by modulations along the y -axis direction. The structural modulations are demonstrated to result from phonon instability, preceding pressure-induced amorphization. The recovered sample after decompression develops a rim of crystalline coesite structure, but its interior remains low crystalline or partially amorphous. Our results not only clarify that the pressure-induced reversible phase transitions and amorphization in coesite originate from structural modulations along the y -axis direction, but also shed light on the densification mechanism of silica under high pressure.

DOI: [10.1103/PhysRevB.98.104106](https://doi.org/10.1103/PhysRevB.98.104106)

I. INTRODUCTION

Silica, SiO₂, as the principal component of the Earth's crust, is of great significance in geoscience and materials science [1]. Despite its simple chemical composition, silica shows rich polymorphism at elevated pressures and temperatures with many stable or metastable phases [2–5]. An understanding of the mechanisms of phase transition between its polymorphs is essential to understand the pressure/temperature behavior of silica and the resultant variations in its properties [6–8]. Coesite, a polymorph of SiO₂, is the densest known polymorph of silica that still retains the tetrahedral coordinated (by oxygen) arrangement of silicon atoms familiar in quartz [9]. Coesite is found in nature in rocks subjected to high pressure, such as the shocked sandstones of meteor-impact craters and certain high-pressure metamorphic rocks. It is widely accepted as a high-pressure indicator in rocks [10]. Coesite can also be synthesized from quartz in the laboratory at 3–9 GPa and high temperature and it undergoes a further phase transition to stishovite at even higher pressure [11–13]. Given its importance in high-pressure mineral physics, it is particularly important to understand the structure features and thermodynamic stability of coesite at high pressure.

Coesite is a framework silicate with corner-sharing SiO₄ tetrahedra arranged in a monoclinic unit cell (space group $C2/c$, $Z = 16$) [14], which is pseudo-hexagonal with almost equal a and c axes, and a β angle close to 120°. Static compression studies conclude that coesite is structurally stable up to 9.6 GPa but highly anisotropic, with the stiffest direction parallel to the chains of tetrahedra along the c axis [15–17]. The dominant mechanism of compression is the reduction of four of the five independent Si-O-Si angles within the structure and the fifth Si1-O1-Si1 angle is constrained to 180° due to symmetry requirements [18]. In addition, spectroscopic experiments and powder x-ray diffraction (XRD) studies at room temperature suggest that coesite transforms to a metastable phase at 22–25 GPa before becoming amorphous above 30 GPa [19–21]. Recently, Černok *et al.* [22,23] reported two phase transitions of coesite on compression by Raman and single-crystal XRD. Instead of becoming amorphous, they reported that coesite remains crystalline up to at least ~ 51 GPa at room temperature. Coesite transforms to a reduced structure (coesite-II: space group $P2_1/n$, $Z = 32$) with a doubled b -cell parameter at ~ 23 GPa and then to a triclinic structure (coesite-III) at ~ 35 GPa. Additionally, these two phase transitions are reversible on decompression and coesite is retrieved after decompressing to ambient pressure. More recently, using single-crystal XRD and theoretical simulations, Hu *et al.* [24] concluded that four triclinic metastable phases bridge the phase transformation from coesite to a post-stishovite structure (space group $P2/c$), and this represents the phase-transition pathway from four-coordinated to

*Corresponding author: yew@whut.edu.cn

†Corresponding author: hanyuli801@gmail.com

‡Corresponding author: satr@cam.ac.uk

six-coordinated silica. Powder XRD results up to ~ 31 GPa by Chen *et al.* [25] confirm a phase transition from coesite to coesite-II occurring at ~ 20 GPa, although the powder x-ray diffraction patterns of coesite-II could not be indexed.

In spite of these extensive experimental and theoretical studies, discrepancies regarding the structural features of coesite at high pressure remain. Pressure-induced amorphization of coesite remains a rather controversial issue. Spectroscopic measurements demonstrated that amorphization of coesite under pressure can be promoted by the presence of large nonhydrostatic stresses [20]. Hemley *et al.* [19] pointed out that amorphization may be driven principally by the elastic instability of coesite upon compression. Dean *et al.* [26] also suggested that coupling between shear instability and phonon softening plays an important role in pressure-induced amorphization. Similarly, the transition from the crystalline to amorphous phase in quartz occurs at a pressure range of 25–30 GPa due to elastic instability [27,28]. Moreover, early studies reported that amorphization of coesite is irreversible upon decompression [19,20], but more recently a reversible crystalline-amorphous transition has been reported [22]. Further disagreement is found regarding descriptions of the transformation pathways of coesite under pressure. A high-pressure structure (coesite-II), distorted with respect to coesite, appears at 20–25 GPa and further transforms to triclinic coesite-III at ~ 35 GPa [23], but four alternative triclinic structures have been reported as intermediate phases of coesite during the transition to post-stishovite [24]. It is worth mentioning that samples in both studies remain crystalline up to ~ 50 GPa rather than transforming to amorphous as reported by Hemley *et al.* [19].

It is clear that the high-pressure behavior of coesite needs to be resolved. Here, we describe an investigation of transformation pathways of coesite on compression and decompression by single-crystal XRD and Raman spectroscopy coupled with the diamond anvil cell (DAC). We find reversible pressure-induced phase transitions and amorphization in coesite, associated with commensurate structural modulations along the y axis of the coesite structure. Theoretical simulations reveal that these are due to phonon instability along the Γ - Y direction of the Brillouin zone. Our study helps resolve the high-pressure behavior and phase-transition mechanisms of coesite.

II. SAMPLE AND EXPERIMENTAL METHODS

A. Sample synthesis and characterizations

Single-crystal coesite was synthesized in a 1500 ton multi-anvil apparatus at the Geophysical Laboratory (GL), Carnegie Institution for Science (Run No. PR1397). The multi-anvil experiment was conducted with a 14/8 (octahedron edge length/truncated edge length) octahedron made from Cr_2O_3 -doped MgO fitted with a ZrO_2 sleeve and a Re heater. Temperature was monitored with a C-type W5%Re-W26%Re thermocouple. The starting material ($\text{SiO}_2 \cdot n\text{H}_2\text{O}$, $n = 0.85$) was sealed in a platinum capsule with outer diameter 2.5 mm and length 3.0 mm. The assembly was cold pressurized to 10 GPa and heated up to 1600 °C for 1 hour, then slow cooled down to 1200 °C at a rate of 2 °C/min. After holding for 2 hours at

10 GPa and 1200 °C, the experiment was quenched to room temperature by turning off the power directly. Finally, pressure was automatically released to ambient pressure. Water-saturated conditions and slow cooling promote the growth of relatively large single crystals [29].

The recovered samples consist of mostly anhedral single crystals, 100–400 μm in diameter. Raman spectroscopy on the recovered sample confirmed that it is coesite. Optically clear single crystals were selected for unpolarized infrared (IR) measurements in order to calculate the water content. Two single crystals were double-sided polished to a thickness of 130 and 195 μm , respectively. The IR measurements were conducted on a JASCO FT/IR-6300 Fourier Transform Infrared Spectrometer at GL. The spectra were obtained from 512 scans over a spatial scan range of $150 \times 150 \mu\text{m}^2$. The unpolarized IR spectrum of the synthesized coesite shows five O-H vibration bands in the region of 2800–4000 cm^{-1} (Fig. S1 of the Supplemental Material [49]). According to the Lambert-Beer law, the intensity of the OH bands in a sample is proportional to its OH concentration: $A_i = \varepsilon_i \cdot t \cdot c$, where A_i is the total integrated absorbance, ε_i is the integrated molar absorption coefficient ($\varepsilon_i = 190\,000 \text{ l mol}^{-1} \text{ cm}^{-2}$) [30], t is the thickness (cm), and c is the water concentration ($\text{mol}_{\text{H}_2\text{O}}/\text{l}$). The calculated water content in the synthesized coesite is $185(\pm 30)$ ppm. This is consistent with earlier studies on the pressure dependence of hydroxyl solubility in coesite, according to which coesite incorporates hydrogen at P - T conditions above 5 GPa and 1000 °C [30,31].

B. Single-crystal x-ray diffraction

High-pressure single-crystal x-ray diffraction experiments were performed at the GeoSoilEnviroConsortium for Advanced Radiation Sources (GSECARS) and the High-Pressure Collaborative Access Team (HPCAT) sectors of the Advanced Photon Source (APS), Argonne National Laboratory (ANL). Monochromatic x-ray beams were used, with wavelength $\lambda = 0.33440 \text{ \AA}$ for GSECARS and $\lambda = 0.40663 \text{ \AA}$ for HPCAT. Experiments were carried out using a symmetric-type DAC equipped with 300 μm culet size diamonds and a preindented rhenium gasket with the thickness ~ 30 -40 μm . A piece of single-crystal coesite with a diameter of $\sim 20 \mu\text{m}$ and a thickness of $\sim 12 \mu\text{m}$ was loaded into a sample chamber of 120 μm diameter. Neon gas was used as the pressure-transmitting medium and fine gold powder was placed next to the crystal for pressure calibration [32]. Step-scan diffraction patterns were collected at each x-ray incident angle from -10° to 10° and a wide-scan image was taken continuously for the same range. Single-crystal diffraction patterns were evaluated to determine the orientation matrix and index d spacings with Miller indices (hkl) using the GSE_ADA and RSV programs [33].

C. Raman spectroscopy

High-pressure Raman spectra were collected using a JASCO NRS-3100 Laser Raman Spectrophotometer at GL. The spectrometer is equipped with holographic gratings, a single monochromator, and a 1024×128 Andor DV401-F1 CCD Peltier-cooled detector operating at -70°C . The

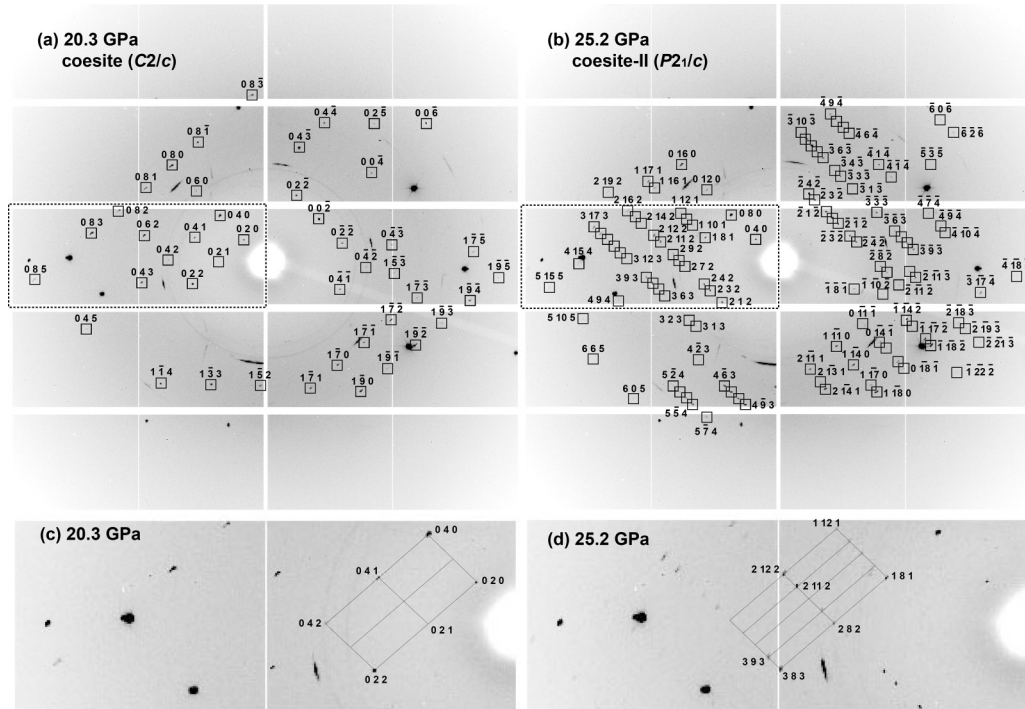


FIG. 1. Indexed x-ray diffraction patterns of coesite at 20.3 and 25.2 GPa. (a) Coesite ($C2/c$) at 20.3 GPa and (b) coesite-II ($P2_1/c$) at 25.2 GPa. (c), (d) Zoomed-in pictures corresponding to the dashed boxes in (a) and (b), respectively. The reciprocal lattice reconstruction is marked in (c) and (d) by grids.

531.8 nm line of a coherent solid-state laser was used for sample excitation, with a power of 6.3 mW at the sample. The spectrometer was calibrated using the silicon peak at 520 cm^{-1} . Raman spectra of the sample were recorded using a 1200 grooves/mm grating with three accumulations, each of an exposure time of 120 seconds. The same type of DAC and Re gasket was used as for the x-ray experiments, with a neon pressure-transmitting medium, while pressure was determined by the fluorescence shift of a ruby sphere placed next to the coesite crystal [34].

D. Theoretical simulations

Structural relaxations were performed using density functional theory (DFT) within the Perdew-Burke-Ernzerhof (PBE) parametrization of the generalized gradient approximation (GGA) [35], as implemented in the Vienna *Ab initio* Simulation Package (VASP) [36]. The all-electron projector augmented-wave (PAW) potentials [37] were used in which the $3s^23p^2$ and $2s^22p^4$ are treated as valence electrons for Si and O atoms, respectively. The Brillouin zone was sampled with Monkhorst-Pack k meshes [38] with the resolution of $2\pi \times 0.04 \text{ \AA}^{-1}$ for all phases.

Phonons in crystals provide definitive indicators of structural stability. We employed the supercell approach as implemented in the PHONOPY code [39] to calculate the phonon dispersion of coesite and its high-pressure phase. According to the crystal symmetry, the finite displacements of the atoms could be generated. Then the Hellmann-Feynman forces could be obtained from the single-point self-consistent total-energy calculation. Once the force constant is determined, the phonon

frequency can be calculated at selected q points along the symmetry lines in the Brillouin zone.

First-principles molecular dynamics (MD) simulations using the canonical NVT (N number of particles, V volume, and T temperature) and NPT (N number of particles, P pressure, and T temperature) ensembles were performed for the coesite structure to examine its thermal stability. The simulation consists of 10 000 steps with an integration time of 1 fs. The self-consistency on the total energy was 1×10^{-5} eV.

III. RESULTS AND DISCUSSION

The combination of XRD with DAC enables us to track the structural behavior of coesite as a function of pressure up to 50 GPa. At pressures below ~ 22 GPa, all diffraction peaks except for saturated diamond peaks and diffraction rings from Ne and Re can be indexed as monoclinic coesite ($C2/c$, $Z = 16$) [Fig. 1(a)]. We observed an abrupt change in the diffraction pattern between ~ 22 and ~ 25 GPa, which is characterized by an increase in the number of diffraction peaks with increasing pressure and an overall decrease in their intensities. This is in agreement with previous Raman spectroscopy and single-crystal XRD observations of a pressure-induced structural transformation in coesite to a lower-symmetry coesite-II [20,22,23]. The diffraction pattern at 25.2 GPa can be indexed according to the coesite-II structure [$P2_1/c$, $Z = 32$, $a = 6.632(3) \text{ \AA}$, $b = 23.321(2) \text{ \AA}$, $c = 6.858(5) \text{ \AA}$, $\beta = 120.1(1)^\circ$, and $V = 917.5(18) \text{ \AA}^3$] [Fig. 1(b)], which is equivalent to the $P2_1/n$ structure reported by Černok *et al.* [23], but with a different cell setting. The enlarged regions of the diffraction patterns at 20.3 and 25.2 GPa show that the

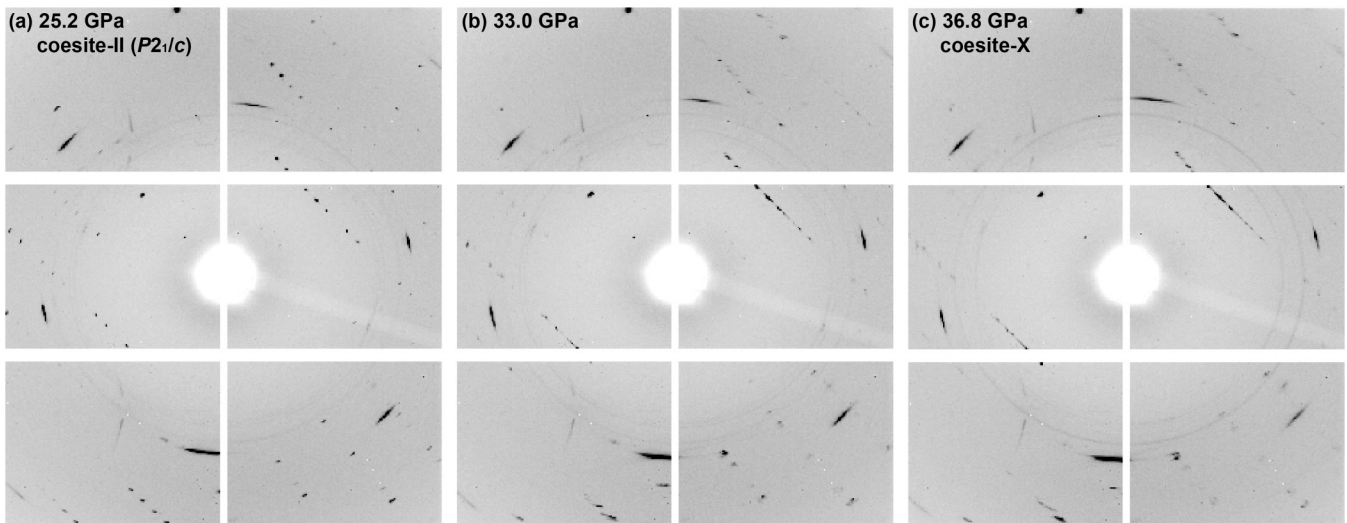


FIG. 2. X-ray diffraction patterns of coesite at (a) 25.2, (b) 33.0, and (c) 36.8 GPa.

b^* reciprocal lattice parameter for coesite-II is half of that for coesite [Figs. 1(c) and 1(d)], which indicates a zone-boundary displacive phase transition from coesite to coesite-II, associated with a doubling of the cell parameter along the y axis of coesite as it transforms to coesite-II. Correspondingly, a doubled unit-cell volume and number of formula units ($Z = 32$) per unit cell are obtained for the coesite-II phase. Coesite-II can be thought of as a commensurate modulated variation of coesite with the modulation wave vector $q = 0.5b^*$ [40].

Above ~ 36 GPa, the intensity of the coesite-II peaks becomes greatly reduced, while unidentified peaks appear

among relatively strong coesite-II peaks (Fig. 2). These new weak peaks also occur along the y^* axis of the coesite-II reciprocal lattice. Specifically, new diffraction intensity appears between $(2\ 2\ 2)$ and $(2\ 3\ 2)$ of the diffraction patterns of the coesite-II structure at 36.8 GPa, as marked by grids in Fig. 3(b). These indicate that the coesite-II structure undergoes commensurate modulation along the y axis at pressures above ~ 36 GPa. We denote the modulated structure as coesite-X since it is different from the coesite-III structure reported by Černok *et al.* [23]. Due to the low crystallinity of sample at pressures above ~ 36 GPa, the coesite-X structure

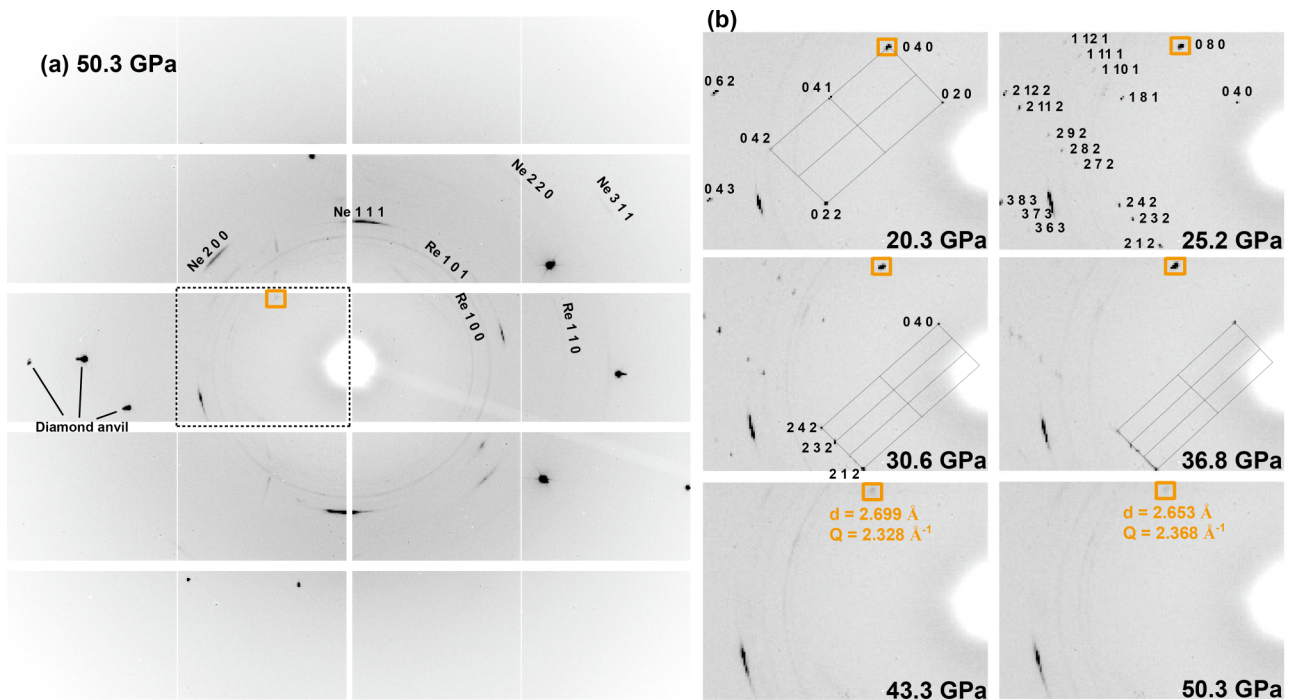


FIG. 3. X-ray diffraction patterns of coesite at high pressures. (a) X-ray diffraction pattern at 50.3 GPa. (b) Zoomed-in pictures corresponding to the dashed box in (a) and track phase transformations of coesite from 20.3 to 50.3 GPa. The diffraction peak marked in the orange box starts from $(0\ 4\ 0)$ of coesite and then $(0\ 8\ 0)$ of coesite-II.

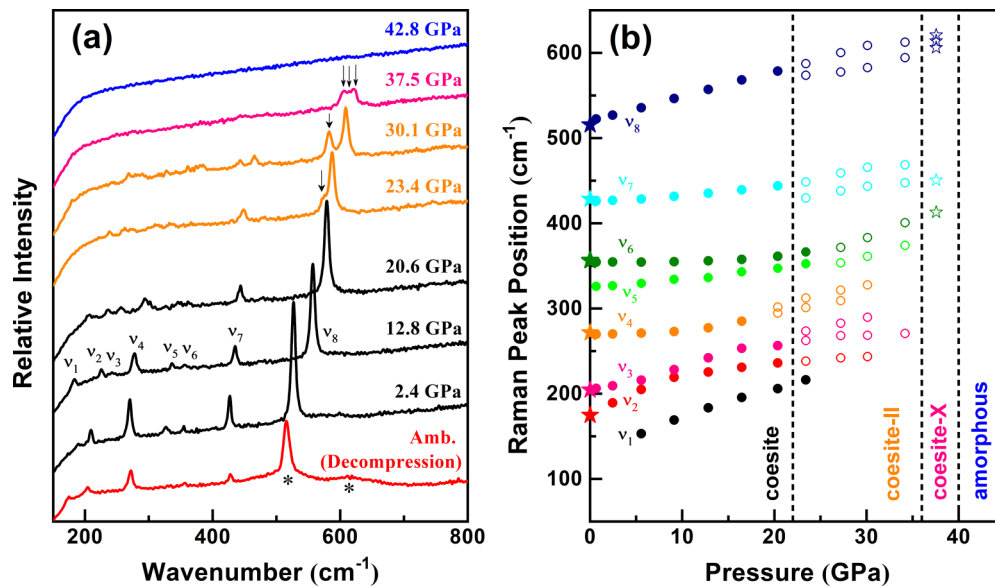


FIG. 4. Raman spectra of (a) coesite and (b) mode frequencies during compression and decompression. The asterisks on the quenched ambient spectrum in (a) indicate two diffuse Raman bands at ~ 520 and ~ 620 cm^{-1} . The solid stars in (b) represent Raman peak positions of the quenched ambient spectrum. The dashed lines in (b) indicate the phase boundaries of polymorphs for coesite.

cannot be indexed and solved. The coesite-X phase does not persist above 40 GPa and we also did not observe any strong diffraction peaks from the original coesite at these pressures (Fig. 3). There is only a broad and weak diffraction intensity occurring originally close to the (0 4 0) peak of coesite and then persisting at higher pressures where this becomes the (0 8 0) peak of coesite-II, as indicated by the orange box in Fig. 3. At 50.3 GPa, this peak with $d = 2.653$ Å (momentum transfer $Q = 2.368$ Å $^{-1}$) coincides with the first sharp diffraction peak (Si-O bond correlation, $Q \sim 2.39$ – 2.40 Å $^{-1}$) of SiO $_2$ glass at ~ 50 GPa [41,42]. These changes indicate that the coesite sample is very weakly crystalline and commences amorphization above ~ 40 GPa.

High-pressure Raman spectra measurements on single-crystal coesite confirm our XRD observations. Coesite shows eight Raman active peaks (ν_1 – ν_8) in the region of 150–800 cm^{-1} with the strongest peak (ν_8) at ~ 519 cm^{-1} assigned to the Si-O-Si stretching mode (Fig. 4). The intensities and positions of these peaks are in good agreement with previous studies [20,22]. All the vibration bands show a continuous positive-pressure shift during compression and can be followed up to ~ 22 GPa. The spectrum changes abruptly between ~ 22 and ~ 25 GPa. The strongest band (ν_8) splits into a doublet, accompanied by similar splitting of three weaker bands (ν_3 , ν_4 , and ν_7). We also note that Raman mode ν_1 disappears gradually at pressures above ~ 22 GPa and two further modes (ν_5 and ν_6) show contrasting pressure dependence below and above ~ 22 GPa. These results are in agreement with those of Hemley [20] and Černok *et al.* [22] and their conclusions. The observed splitting of Raman modes suggests that a phase transformation occurs at 22–25 GPa and that this is accompanied by a distortion of the coesite structure. The new phase has been confirmed as a coesite-II structure by means of single-crystal XRD in this study and that of Černok *et al.* [23]. The Raman spectra weaken and broaden

at pressures above ~ 36 GPa. At 37.5 GPa, a triplet near 600 cm^{-1} was observed, indicating that the coesite-II structure further transforms to another distorted structure, coesite-X, as suggested by our single-crystal XRD. All Raman peaks disappeared at the highest pressure of 42.8 GPa. This suggests that the sample is very weakly crystalline and amorphization starts above ~ 40 GPa, supported by our single-crystal XRD data above.

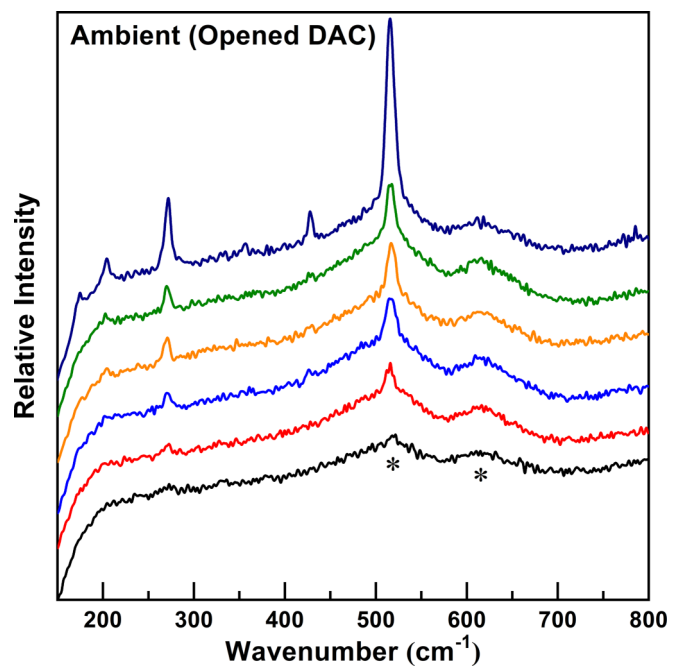


FIG. 5. Raman spectra collected at different positions within the recovered sample after decompression from 42.8 GPa to ambient conditions. The asterisks indicate two diffuse Raman bands at ~ 520 and ~ 620 cm^{-1} .

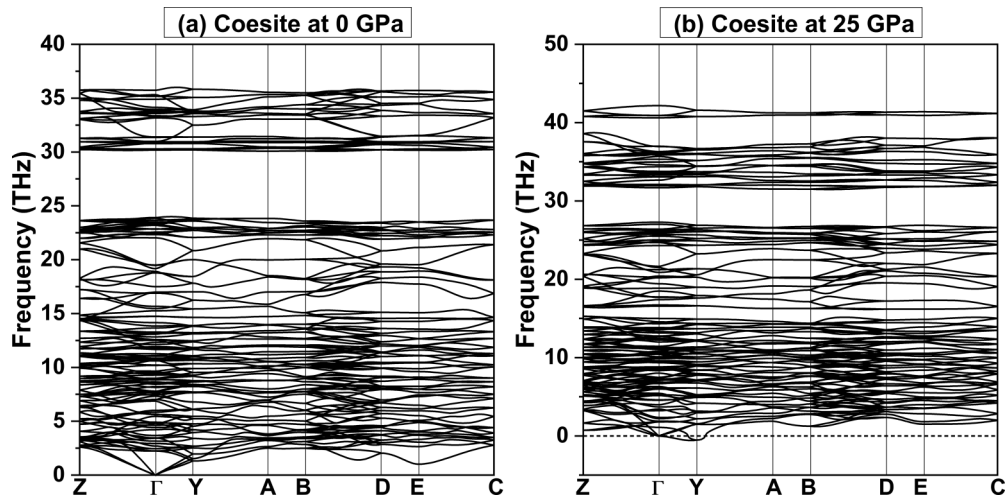


FIG. 6. Phonon dispersion curves of coesite ($C2/c$) at (a) 0 and (b) 25 GPa.

Upon decompression to ambient pressure, an interesting phenomenon is observed in the recovered sample. The recovered sample develops a rim of a back-transformed coesite phase, but its interior remains very low crystalline or amorphous. All spectra of the pressure-quenched coesite from 42.8 GPa exhibit two diffuse Raman bands at ~ 520 and $\sim 620 \text{ cm}^{-1}$, marked with asterisks in Figs. 4(a) and 5, which are also observed for quartz and silica glass quenched from high pressure [20,43]. Decompression from 42.8 GPa is accompanied by recrystallization of the coesite structure and partial preservation of the low-crystalline or amorphous phase. Shear stresses concentrated at the boundary between the sample and the pressure medium could well play an important role in the transformation during the decompression. Similar features of recrystallization and reversible amorphization during decompression have also been observed on berlinite and zeolites under quasi-hydrostatic conditions [44–46].

To further elucidate the phase-transition mechanism of coesite at high pressure, we performed first-principles simulations based on DFT. According to previous studies, phonon softening plays an important role in the phase transition and amorphization of quartz under pressure [47]. Similar pressure-induced behaviors occur in coesite according to our experimental results. Here, a $2 \times 1 \times 2$ coesite supercell with 192 atoms was employed. Coesite is dynamically stable at 0 GPa since there is no imaginary phonon mode across the entire Brillouin zone [Fig. 6(a)], validating our computational scheme. However, imaginary vibrational modes are found along the Γ - Y direction of the Brillouin zone at 25 GPa [Fig. 6(b)], indicating that by this point the coesite structure is dynamically unstable.

It is noteworthy that the instability mode occurs at the Y zone-boundary point (00.50), suggesting that the wavelength of the unstable vibrational mode corresponds to doubling along the y axis in real space. Therefore, we doubled the y axis of our computational coesite cell and gradually moved the atoms along the unstable vibrational eigenvectors (Fig. 7). The coesite structure tends to become unstable with increasing the atomic displacement and the energy is lowest at a displacement amplitude of 0.015. Full geometry optimization at this

displacement point at 25 GPa results in the coesite-II structure ($P2_1/c$, $Z = 32$) with a doubled b axis with respect to coesite.

The coesite-II ($P2_1/c$) phase has almost identical enthalpy to that of coesite below 20 GPa (Fig. 8). Above 20 GPa, the coesite-II phase becomes thermodynamically stable over coesite as suggested by its relatively lower enthalpy. Moreover, the difference of enthalpy between coesite and $P2_1/c$ structures increases with increasing pressure. These results support the idea that the phase transition from coesite to coesite-II observed experimentally is driven by acoustic softening at the Y point (00.50) of the coesite Brillouin zone and suggest that this phase transition is a typical ferroelastic-related symmetry-breaking transition, potentially second order in character.

Phonon calculations show that the coesite-II structure is dynamically stable at 20 GPa without phonon softening

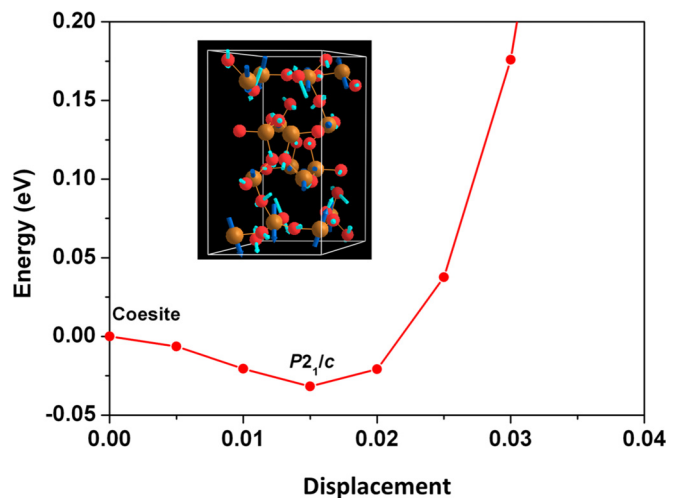


FIG. 7. The energy of coesite with the increased atomic displacement. Atomic displacement is defined as the proportion of atomic amplitude. Blue and cyan arrows represent the directions of displacement for Si and O atoms, respectively, along the unstable vibrational eigenvectors.

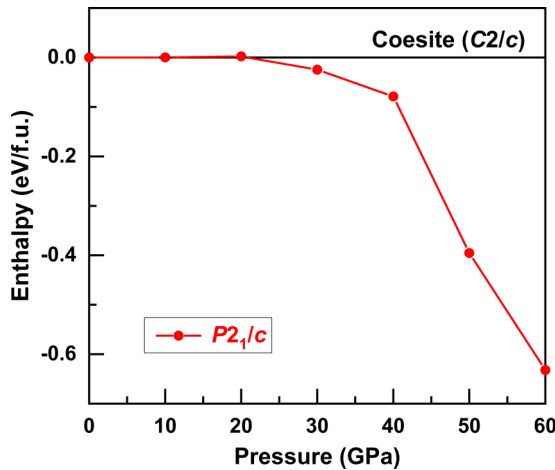


FIG. 8. The relative enthalpies of coesite ($C2/c$) and coesite-II ($P2_1/c$) structures at high pressures.

[Fig. 9(a)]. It is interesting to note that vibrational modes along the Γ -Y direction are imaginary at 40 GPa [Fig. 9(b)], indicating that at this pressure the coesite-II structure is dynamically unstable. Our calculated phonon softening along the Γ -Y direction suggests that the coesite-II structure may undergo further structural modulation along its y axis.

To further examine the thermodynamic stability of coesite, we carried out MD simulations at 300 K using the canonical NVT ensemble. A $2 \times 2 \times 2$ supercell of coesite with 384 atoms was employed. We found that coesite transforms to a new $P2_1/c$ structure with 96 atoms per unit cell at 30 GPa, which supports our single-crystal XRD results and the theoretical calculations of phonon dispersion and structural relaxations in this study. At 50 GPa, the coesite structure becomes a long-range disordered structure and contains multiple coordination states of silicon, with 4-, 5-, and 6-coordinated Si atoms (Fig. S2 of the Supplemental Material [49]). A $1 \times 4 \times 1$ supercell of coesite-II ($P2_1/c$) with 384 atoms was employed to further explore the size effects along its y axis. At 40 GPa and 300 K, a new modulated structure (labeled coesite-XI), corresponding to modulation along the

y axis of coesite-II, is found and its b -cell parameter is $\sim 90 \text{ \AA}$ (four times the b -cell parameter of coesite-II). The structure information of coesite-XI is presented in the Supplemental Material [49]. As shown in Movie S1 of the Supplemental Material [49], the coesite-XI structure appears as a wave along its y axis. These theoretical results confirm that coesite transforms to modulated structures, with structural modulation along the y axis under high pressure, and that this triggers amorphization at higher pressure.

To further examine the pressure-induced structural modulation mechanism, single-crystal XRD experiments were also performed on coesite up to 54.0 GPa using argon as the pressure-transmitting media. Argon media provide less hydrostatic conditions than neon media. Selected representative XRD patterns are shown in Fig. S3 of the Supplemental Material [49]. The phase transition from coesite to coesite-II occurs at pressures around 22–24 GPa. With increasing pressure, the coesite-II phase undergoes further structural modulation along its y axis. There are only a few weak diffraction peaks up to 54.0 GPa, suggesting that the coesite tends towards amorphization at higher pressure. These results elucidate that the pressure-induced structural modulations in coesite along its y axis are independent of the pressure-transmitting media used.

The phase transition from coesite to coesite-II at ~ 25 GPa is confirmed by means of both experimental and theoretical studies in this and previous studies [20,23]. Four intermediate phases at ~ 26 GPa reported by Hu *et al.* [24] can be related to the coesite-II structure since their reported XRD patterns at ~ 26 GPa display features of a modulated structure, with a main peak surrounded by several satellite peaks. Although helium was used as the pressure-transmitting medium in their studies, both neon and helium media provide good hydrostatic conditions in the DAC at pressures below 30 GPa, with typical deviatoric stress of less than 0.25 GPa [48]. At pressures above 35 GPa, we did not observe phase transitions from either coesite-II to triclinic coesite-III or intermediate phases to monoclinic post-stishovite [23,24], but rather we found modulated structures (coesite-X and coesite-XI), showing structural modulations along the y axis of coesite-II, which

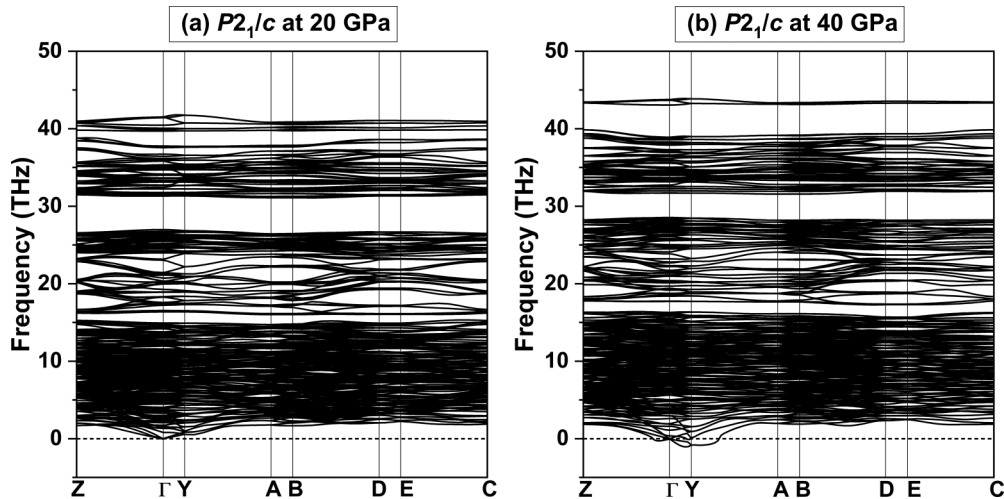


FIG. 9. Phonon-dispersion curves of coesite-II ($P2_1/c$) at (a) 20 GPa and (b) 40 GPa.

precedes amorphization. The amorphous phase of coesite has a long-range disordered structure with 4-, 5-, and 6-coordinated Si atoms at 50 GPa and 300 K based on our MD simulations, which may be considered as an intermediate state towards the octahedrally coordinated post-stishovite phase proposed by Hu *et al.* [24] seen under hydrostatic conditions.

Pressure-induced reversible phase transitions and amorphization in coesite have been observed in this study. The two phase transitions from coesite to coesite-II and then to coesite-III are also reversible, although amorphization is absent in the study of Černok *et al.* [22]. The reversibility of the crystal-to-crystal phase transitions is completely consistent with the symmetry-breaking phonon-softening ferroelastic transitions that we see, and reflects the fact that the polymorphs at high pressure have group-subgroup relationships with this coesite family of structures. Our combined experimental results and theoretical simulations indicate that coesite-II as a commensurate modulated structure of coesite undergoes further modulation along its y axis until, eventually, the long-range crystalline-ordered structure collapses. The high-pressure modulated structures (coesite-II and coesite-X) are distorted relative to the coesite structure and can be considered as precursors to amorphization. The modulation transition mechanism is reversible upon decompression, as has been verified by both our Raman measurements and those of Černok *et al.* [22].

IV. CONCLUSIONS

Pressure-induced structural modulations in coesite have been observed experimentally and confirmed theoretically. Coesite transforms to a distorted coesite-II structure at 22–25 GPa, with a doubled b axis with respect to coesite. The coesite-II structure undergoes further structural modulation

along its y axis at 36–40 GPa and starts amorphization above ~ 40 GPa under quasihydrostatic conditions. These modulation-induced phase and amorphization transitions are reversible experimentally. Theoretical calculations confirm that the modulation wavelength increases along the y axis of coesite upon compression and we have proposed a modulated structure (coesite-XI) that results from modulation along the y axis of coesite-II. Phonon instability plays a key role in driving the phase-modulated transformations in coesite which precede amorphization. A mechanism of pressure-induced phase transitions and amorphization in coesite originating from structural modulations along the y -axis direction is proposed based on our experimental and theoretical results.

ACKNOWLEDGMENTS

We thank Bjorn O. Mysen and Renbiao Tao for experimental assistance, Sergey N. Tkachev for loading the gas medium, and Przemek Dera for helpful discussion. Y.W. acknowledges the financial support from the National Science Foundation of China (Grant No. 41602036) and the program of China Scholarship Council (Grant No. 201606955099). H.L. acknowledges support by EFree, an Energy Frontier Research Center funded by the U.S. Department of Energy, Office of Science, Basic Energy Sciences under Award No. DE-SC-0001057. S.A.T.R. acknowledges the support of the UK Natural Environment Research Council under Grant No. NE/P012167/1. High-pressure XRD experiments were performed at GSECARS of the APS, ANL. GSECARS is supported by the NSF-Earth Sciences (Grant No. EAR-1128799) and the DOE-Geosciences (Grant No. DE-FG02-94ER14466). APS is a U.S. Department of Energy Office of Science User Facility operated for the U.S. DOE Office of Science by ANL under Contract No. DEAC02-06CH11357.

-
- [1] P. J. Heaney, C. T. Prewitt, and G. V. Gibbs, *Silica: Physical Behavior, Geochemistry, and Materials Applications*, Reviews in Mineralogy and Geochemistry, Vol. 29 (Mineralogical Society of America, Chantilly, Virginia, 1994), p. 606.
 - [2] R. J. Hemley, C. T. Prewitt, and K. J. Kingma, *Rev. Mineral. Geochem.* **29**, 41 (1994).
 - [3] Y. Tsuchida and T. Yagi, *Nature (London)* **347**, 267 (1990).
 - [4] K. J. Kingma, R. J. Hemley, H.-k. Mao, and D. R. Veblen, *Phys. Rev. Lett.* **70**, 3927 (1993).
 - [5] J. Haines, J. M. Léger, F. Gorelli, and M. Hanfland, *Phys. Rev. Lett.* **87**, 155503 (2001).
 - [6] L. Huang, M. Durandurdu, and J. Kieffer, *Nat. Mater.* **5**, 977 (2006).
 - [7] R. Martonák, D. Donadio, A. R. Oganov, and M. Parrinello, *Nat. Mater.* **5**, 623 (2006).
 - [8] Y. Liang, C. R. Miranda, and S. Scandolo, *Phys. Rev. Lett.* **99**, 215504 (2007).
 - [9] L. Coes, *Science* **118**, 131 (1953).
 - [10] E. C. Chao, E. M. Shoemaker, and B. M. Madsen, *Science* **132**, 220 (1960).
 - [11] S. Stishov and S. Popova, *Geokhimiya* **10**, e841 (1961).
 - [12] M. Akaogi, H. Yusa, K. Shiraiishi, and T. Suzuki, *J. Geophys. Res. Solid Earth* **100**, 22337 (1995).
 - [13] S. Ono, T. Kikegawa, Y. Higo, and Y. Tange, *Phys. Earth Planet. Inter.* **264**, 1 (2017).
 - [14] G. Gibbs, *Z. Kristallogr. Crystal. Mater.* **145**, 108 (1977).
 - [15] R. Angel, J. Mosenfelder, and C. Shaw, *Phys. Earth Planet. Inter.* **124**, 71 (2001).
 - [16] L. Levien and C. T. Prewitt, *Am. Mineral.* **66**, 324 (1981).
 - [17] H. Kimizuka, S. Ogata, and J. Li, *J. Appl. Phys.* **103**, 053506 (2008).
 - [18] R. Angel, C. Shaw, and G. Gibbs, *Phys. Chem. Miner.* **30**, 167 (2003).
 - [19] R. Hemley, A. Jephcoat, H. K. Mao, L. Ming, and M. Manghnani, *Nature (London)* **334**, 52 (1988).
 - [20] R. Hemley, in *High-Pressure Research in Mineral Physics: A Volume in Honor of Syun-iti Akimoto*, AGU Geophysical Monograph Series, Vol. 39, edited by M. H. Manghnani, and Y. Syono (Terra Scientific Publishing Company (TERRAPUB), Tokyo, 1987), p. 347.
 - [21] Q. Williams, R. Hemley, M. Kruger, and R. Jeanloz, *J. Geophys. Res. Solid Earth* **98**, 22157 (1993).
 - [22] A. Černok, T. B. Ballaran, R. Caracas, N. Miyajima, E. Bykova, V. Prakapenka, H.-P. Liermann, and L. Dubrovinsky, *Am. Mineral.* **99**, 755 (2014).

- [23] A. Černok, E. Bykova, T. B. Ballaran, H.-P. Liermann, M. Hanfland, and L. Dubrovinsky, *Z. Kristallograph. Crystal. Mater.* **229**, 761 (2014).
- [24] Q. Y. Hu, J.-F. Shu, A. Cadien, Y. Meng, W. G. Yang, H. W. Sheng, and H.-K. Mao, *Nat. Commun.* **6**, 6630 (2015).
- [25] T. Chen, X. Wang, X. Qi, M. Ma, Z. Xu, and B. Li, *Am. Mineral.* **101**, 1190 (2016).
- [26] D. W. Dean, R. M. Wentzcovitch, N. Keskar, J. R. Chelikowsky, and N. Binggeli, *Phys. Rev. B* **61**, 3303 (2000).
- [27] N. Binggeli and J. R. Chelikowsky, *Phys. Rev. Lett.* **69**, 2220 (1992).
- [28] K. J. Kingma, C. Meade, R. J. Hemley, H.-k. Mao, and D. R. Veblen, *Science* **259**, 666 (1993).
- [29] A. Shatskiy, D. Yamazaki, Y. M. Borzdov, T. Matsuzaki, K. D. Litasov, T. Cooray, A. Ferot, E. Ito, and T. Katsura, *Am. Mineral.* **95**, 135 (2010).
- [30] M. Koch-Müller, Y. Fei, E. Hauri, and Z. Liu, *Phys. Chem. Miner.* **28**, 693 (2001).
- [31] J. Mosenfelder, *Phys. Chem. Miner.* **27**, 610 (2000).
- [32] Y. Fei, A. Ricolleau, M. Frank, K. Mibe, G. Shen, and V. Prakapenka, *Proc. Natl. Acad. Sci.* **104**, 9182 (2007).
- [33] P. Dera, K. Zhuravlev, V. Prakapenka, M. L. Rivers, G. J. Finkelstein, O. Grubor-Urosevic, O. Tschauner, S. M. Clark, and R. T. Downs, *High Pressure Res.* **33**, 466 (2013).
- [34] H. K. Mao, J. Xu, and P. M. Bell, *J. Geophys. Res.* **91**, 4673 (1986).
- [35] J. P. Perdew, K. Burke, and M. Ernzerhof, *Phys. Rev. Lett.* **77**, 3865 (1996).
- [36] G. Kresse and J. Furthmüller, *Phys. Rev. B* **54**, 11169 (1996).
- [37] G. Kresse and D. Joubert, *Phys. Rev. B* **59**, 1758 (1999).
- [38] H. J. Monkhorst and J. D. Pack, *Phys. Rev. B* **13**, 5188 (1976).
- [39] A. Togo, F. Oba, and I. Tanaka, *Phys. Rev. B* **78**, 134106 (2008).
- [40] T. Janssen, A. Janner, A. Looijenga-Vos, and P. De Wolff, in *International Tables for Crystallography Volume C: Mathematical, Physical and Chemical Tables* (Springer, New York, 2006), p. 907.
- [41] T. Sato and N. Funamori, *Phys. Rev. B* **82**, 184102 (2010).
- [42] T. Sato and N. Funamori, *Phys. Rev. Lett.* **101**, 255502 (2008).
- [43] R. J. Hemley, H. K. Mao, P. M. Bell, and B. O. Mysen, *Phys. Rev. Lett.* **57**, 747 (1986).
- [44] P. Gillet, J.-M. Malezieux, and J.-P. Itie, *Am. Mineral.* **81**, 651 (1996).
- [45] T. D. Bennett, P. Simoncic, S. A. Moggach, F. Gozzo, P. Macchi, D. A. Keen, J.-C. Tan, and A. K. Cheetham, *Chem. Commun.* **47**, 7983 (2011).
- [46] P. Gillet, J. Badro, B. Varrel, and P. F. McMillan, *Phys. Rev. B* **51**, 11262 (1995).
- [47] N. Choudhury and S. L. Chaplot, *Phys. Rev. B* **73**, 094304 (2006).
- [48] S. Klotz, J. C. Chervin, P. Munsch, and G. Le Marchand, *J. Phys. D: Appl. Phys.* **42**, 075413 (2009).
- [49] See Supplemental Material at <http://link.aps.org/supplemental/10.1103/PhysRevB.98.104106> for infrared data, molecular dynamics results for silicon coordination numbers, x-ray diffraction data, and detailed structural information.